Supporting Information

Simulating Graphene Oxide Nanomaterial Phototransformation and Transport in Surface Water

Yanlai Han,[*a,b] Christopher D. Knightes,[*b] Dermont Bouchard,[b] Richard Zepp,[b] Brian Avant,[a,b] Hsin-Se Hsieh,[c,b] Xiaojun Chang,[c,b] Brad Acrey,[a,b] W. Matthew, Henderson,[b] Jessica Spear.[a,b]

[a]Oak Ridge Institute for Science and Education

[b]U.S. Environmental Protection Agency, Office of Research and Development, National Exposure Research Laboratory, Athens, GA 30605, USA

[c]National Research Council Research Associate

* Corresponding authors:
Christopher D. Knightes, phone: +1(706)355 8326, email: knightes.chris@epa.gov
Yanlai Han, phone: +1(706)355 8151, email: han.yanlai@epa.gov

1. Brier Creek WASP8 model

1.1 Brier Creek river model implementation in WASP8

WASP8 input parameters of Brier Creek river include river segmentation; river geometry; segment inflow and initial velocity; sediment solids particle sizes and densities; initial suspended solids concentration, sediment concentration, and resuspension rate of sediment in each segment. WASP8 internally calculates hydraulic residence time, outflow, settling velocity of suspended solids, and sediment burial rate in each segment.

The Brier Creek river model was established by Bouchard et al.[1] using WASP8, and adjusted for this study. WASPBuilder, a plugin of BASIN4.0, was applied for river segmentation and parameterization. River delineation was performed in BASINS using a 10m NED and spatial threshold of 96 km^2. The final Brier Creek watershed study area is 1709 km^2 containing 3% impervious and 97% pervious surface area. This model was divided into 14 sub-basins including two tributaries and 12 sub-basins on the mainstream. Sub-basin areas ranged from 50 to 130 km^2. Using WASPBuilder, an NHDPlus Flowline layer was simplified and then divided into sections for each of the 14 sub-basins. Each segment was divided into three compartments vertically, including water column, surface sediment layer (benthic sediment) and subsurface sediment layer (deep sediment).

The flow routing transport mode is used in Brier Creek. Daily flowrate data were retrieved from USGS gage 02197830 (Brier Creek near Waynesboro, GA) during the period from 01/01/1992-12/31/1999, because daily flowrate is only available during this period. HSPF was used to calibrate the flowrate to the observed data from USGS gage 02197830 in segment 8, and then the flowrate in each segment of the watershed could be calculated by HSPF. For mean flow conditions, flowrate in each segment during this period was averaged and was implemented into WASP8. For low flow conditions, lowest flow condition in each segment was selected, and then input into WASP8.

Table S1 and S2 displays the initial velocity and segment inflow for each segment in WASP8 at mean flow and low flow conditions, which are WASP8 input parameters. Once flow enters a segment, it flows downstream with the rest of the inputs until it leaves the system. WASP8 internally calculates segment outflows and hydraulic residence times, which are presented in Table S1 and S2.

Table S1 Geometry parameters, flow rate, and residence time in each segment for Brier Creek at the mean flow condition. WC represents water column, SB represents surface sediment, SSB represents subsurface layer. Same number indicates the same segment. For example, SB_1 is beneath WC_1, and SSB_1 is beneath SB_1.

Segment Names	Volume [m^3]	Initial Depth [m]	Initial Velocity [$m\ s^{-1}$]	Segment Inflow [$m^3\ s^{-1}$]	Segment Outflow [$m^3\ s^{-1}$]	Residence Time (d)
WC_1	20,397	1.73	0.31	2.10	2.10	0.112
WC_2	33,083	2.30	0.35	0.79	2.89	0.132

Segment Names	Volume [m^3]	Initial Depth [m]	Initial Velocity [$m\ s^{-1}$]	Segment Inflow [$m^3\ s^{-1}$]	Segment Outflow [$m^3\ s^{-1}$]	Residence Time (d)
WC_3	36,551	2.41	0.32	1.04	3.93	0.108
WC_4	67,245	2.58	0.36	0.83	4.76	0.164
WC_5	58,605	2.80	0.33	0.66	5.42	0.125
WC_6	127,845	3.06	0.4	0.42	6.88	0.215
WC_7	222,393	3.30	0.42	1.19	9.13	0.282
WC_8	247,040	3.40	0.4	1.12	10.25	0.279
WC_9	217,025	3.42	0.4	1.28	11.53	0.218
WC_10	177,740	3.57	0.44	0.94	12.47	0.165
WC_11	294,862	3.64	0.44	1.11	13.58	0.251
WC_12	416,407	3.73	0.43	1.20	14.78	0.326
Reedy_WC	28,609	1.79	0.3	1.04	4.46	0.318
Brushy_WC	21,046	1.85	0.31	1.06	7.94	0.230
SB_1	1,180	0.05	0	0	0	0
SB_2	1,440	0.05	0	0	0	0
SB_3	1,517	0.05	0	0	0	0
SB_4	2,604	0.05	0	0	0	0
SB_5	2,089	0.05	0	0	0	0
SB_6	4,183	0.05	0	0	0	0
SB_7	6,746	0.05	0	0	0	0
SB_8	7,261	0.05	0	0	0	0
SB_9	6,339	0.05	0	0	0	0
SB_10	4,973	0.05	0	0	0	0
SB_11	8,092	0.05	0	0	0	0
SB_12	11,176	0.05	0	0	0	0
Reedy_SB	1,601	0.05	0	0	0	0
Brushy _SB	1,140	0.05	0	0	0	0
SSB_1	3,540	0.15	0	0	0	0
SSB_2	4,321	0.15	0	0	0	0
SSB_3	4,551	0.15	0	0	0	0
SSB_4	7,813	0.15	0	0	0	0
SSB_5	6,268	0.15	0	0	0	0
SSB_6	12,548	0.15	0	0	0	0
SSB_7	20,238	0.15	0	0	0	0
SSB_8	21,783	0.15	0	0	0	0
SSB_9	19,017	0.15	0	0	0	0
SSB_10	14,919	0.15	0	0	0	0
SSB_11	24,277	0.15	0	0	0	0
SSB_12	33,529	0.15	0	0	0	0
Reedy _SSB	4,802	0.15	0	0	0	0
Brushy _SSB	3,421	0.15	0	0	0	0

Table S2 Geometry parameters, flow rate, and residence time in each segment for Brier Creek at low flow condition.

Segment Names	Volume [m^3]	Initial Depth [m]	Initial Velocity [$m\ s^{-1}$]	Segment Inflow [$m^3\ s^{-1}$]	Segment Outflow [$m^3\ s^{-1}$]	Residence Time (d)
WC_1	12026	1.02	0.10	0.12	0.12	1.160
WC_2	17548	1.22	0.14	0.05	0.17	1.195
WC_3	19565	1.29	0.14	0.06	0.23	0.985
WC_4	34926	1.34	0.15	0.05	0.28	1.144
WC_5	28465	1.36	0.18	0.07	0.35	0.941
WC_6	58073	1.39	0.4	0.03	0.40	1.680
WC_7	95022	1.41	0.42	0.06	0.49	2.244
WC_8	104629	1.44	0.4	0.03	0.52	2.329
WC_9	92648	1.46	0.4	0.03	0.55	1.950
WC_10	73685	1.48	0.44	0.02	0.57	1.496
WC_11	120699	1.49	0.44	0.03	0.60	2.328
WC_12	168572	1.51	0.43	0.03	0.63	3.097
Reedy_WC	15823	0.99	0.3	0.02	0.02	9.157
Brushy_WC	11376	1.00	0.31	0.03	0.03	4.389
SB_1	1,180	0.05	0	0	0	0
SB_2	1,440	0.05	0	0	0	0
SB_3	1,517	0.05	0	0	0	0
SB_4	2,604	0.05	0	0	0	0
SB_5	2,089	0.05	0	0	0	0
SB_6	4,183	0.05	0	0	0	0
SB_7	6,746	0.05	0	0	0	0
SB_8	7,261	0.05	0	0	0	0
SB_9	6,339	0.05	0	0	0	0
SB_10	4,973	0.05	0	0	0	0
SB_11	8,092	0.05	0	0	0	0
SB_12	11,176	0.05	0	0	0	0
Reedy_SB	1,601	0.05	0	0	0	0
Brushy _SB	1,140	0.05	0	0	0	0
SSB_1	3,540	0.15	0	0	0	0
SSB_2	4,321	0.15	0	0	0	0
SSB_3	4,551	0.15	0	0	0	0
SSB_4	7,813	0.15	0	0	0	0
SSB_5	6,268	0.15	0	0	0	0
SSB_6	12,548	0.15	0	0	0	0
SSB_7	20,238	0.15	0	0	0	0
SSB_8	21,783	0.15	0	0	0	0
SSB_9	19,017	0.15	0	0	0	0
SSB_10	14,919	0.15	0	0	0	0
SSB_11	24,277	0.15	0	0	0	0
SSB_12	33,529	0.15	0	0	0	0

Segment Names	Volume [m^3]	Initial Depth [m]	Initial Velocity [$m\ s^{-1}$]	Segment Inflow [$m^3\ s^{-1}$]	Segment Outflow [$m^3\ s^{-1}$]	Residence Time (d)
Reedy _SSB	4,802	0.15	0	0	0	0
Brushy _SSB	3,421	0.15	0	0	0	0

Suspended solids and sediment data were retrieved from USGS stations 02197830 (Brier Creek near Waynesboro, GA) and 02198000 (Brier Creek at Millhaven, GA), and locations of these two stations are shown in Fig. 1 in the paper. This study uses solids ratios from 02198000 and a porosity of 0.8.[2] We calculated initial conditions in the sediments for sand, silt, and clay. Boundary conditions for silt and clay were calculated by averaging suspended solids and sediment data for all sample dates from station 02197830 and partitioning based on the ratios in the sediments. These concentrations agreed with a USGS report on Georgia streams.[3]

Particulate Organic Matter (POM) was calculated using data downloaded from the Storage and Retrieval (STORET) database from EPA. Total Organic Carbon (TOC) measurements from Georgia Environmental Protection Division (GAEPD) stations 1012801 (Brier Creek at SR 56 near Waynesboro) and 1013001 (Brier Creek – Millhaven) were combined and averaged to give an average POM of 6.68 mg L^{-1} for the sample period. Settling rates of different solids were calculated using Stokes' law and resuspension was set at 2.0E-05 m d^{-1} for all solids. Deposition rates are defined as 50 percent of the settling rate. These values represent the fraction of settling particles that actually deposit to the sediment layer. The calculated settling velocity of sand is 1239377 m d^{-1}, which is six orders of magnitude higher than the other three particles' settling velocity. Therefore, sand immediately settles to the sediment layer. We treat settling velocity and resuspension velocity of sand as zero. Sand load coming into the system is directly loaded to the sediment layer, bypassing the water column. Table S3 presents deposition and resuspension rates of solids in the Brier Creek WASP model.

Table S3 Diameter, density and deposition rate of suspended solids in the water column, and resupension rate from the surface sediment.

Solid Type	WASP Particle Diameter [mm]	Density [$g\ cm^{-3}$]	Settling Velocity [$m\ d^{-1}$]	Deposition Rate [$m\ d^{-1}$]	Resuspension Rate [$m\ d^{-1}$]
Sand	4.031	2.65	0	0	0
Silt	0.006	2.65	2.80	1.40	2.0E-05
Clay	0.002	2.65	0.32	0.16	2.0E-05
POM	0.005	1.5	0.50	0.25	2.0E-05

As solids settle to the sediment layer, sediments are buried into the subsurface sediment. For the subsurface sediment layer, the solid mass received from surface sediment layer is pushed out of the

subsurface sediment and is treated as a loss from the system. WASP8 internally calculates the burial velocity in the surface sediment and in subsurface sediment.

300 kg d^{-1} load of sand is added to each surface sediment segment to maintain sediment concentration ratios similar to USGS station 02198000. Before running our nanomaterial simulations, the Brier Creek WASP8 model was run for the sediment solids concentrations to reach steady state. Table S4 shows the steady state concentration of each solid type, which were then used as initial conditions for the study simulations.

Table S4 Initial concentrations of sand, silt, clay, and POM in the water column and two sediment layers

Segment Name	Sand [mg L^{-1}]	Silt [mg L^{-1}]	Clay [mg L^{-1}]	POM [mg L^{-1}]	DOC [Carbon mg L^{-1}]
WC 1	0.00	1.85	9.60	6.63	5.6
WC_2	0.00	1.80	9.57	6.59	5.6
WC 3	0.00	1.77	9.56	6.58	5.6
WC_4	0.00	1.74	9.53	6.55	5.6
WC 5	0.00	1.71	9.52	6.53	5.6
WC_6	0.00	1.68	9.50	6.51	5.6
WC 7	0.00	1.68	9.50	6.51	5.6
WC_8	0.00	1.67	9.49	6.50	5.6
WC 9	0.00	1.67	9.49	6.50	5.6
WC_10	0.00	1.66	9.48	6.49	5.6
WC 11	0.00	1.65	9.48	6.49	5.6
WC_12	0.00	1.65	9.47	6.48	5.6
Reedy WC	0.00	1.71	9.51	6.53	5.6
Brushy_WC	0.00	1.76	9.55	6.57	5.6
SB 1	476,279	24,012	13,823	15,387	0
SB_2	465,455	29,004	17,126	19,025	0
SB3	459,193	31,564	18,870	20,942	0
SB_4	445,217	37,726	22,942	25,428	0
SB 5	453,097	34,350	21,158	23,427	0
SB_6	433,898	40,391	25,328	28,003	0
SB 7	419,672	46,864	29,380	32,482	0
SB_8	419,672	46,558	29,341	32,425	0
SB 9	426,667	44,671	28,185	31,144	0
SB_10	426,667	44,241	28,046	30,978	0
SB 11	419,672	46,526	29,587	32,672	0

Segment Name	Sand [mg L^{-1}]	Silt [mg L^{-1}]	Clay [mg L^{-1}]	POM [mg L^{-1}]	DOC [Carbon mg L^{-1}]
SB_12	412,903	49,285	31,430	34,698	0
Reedy SB	459,193	30,752	18,979	21,006	0
Brushy _SB	474,074	24,478	14,695	16,302	0
SSB 1	474,788	23,990	13,812	15,374	0
SSB_2	464,048	28,925	17,080	18,975	0
SSB 3	461,608	31,695	18,949	21,029	0
SSB_4	445,540	37,727	22,943	25,429	0
SSB 5	452,764	34,302	21,129	23,394	0
SSB_6	433,898	40,445	25,362	28,041	0
SSB 7	420,822	46,951	29,435	32,543	0
SSB_8	420,823	46,709	29,437	32,531	0
SSB 9	425,485	44,618	28,153	31,108	0
SSB_10	429,050	44,407	28,151	31,094	0
SSB 11	419,674	46,600	29,635	32,725	0
SSB_12	412,944	49,287	31,434	34,701	0
Reedy SSB	461,261	30,868	19,049	21,084	0
Brushy SSB	472,071	24,391	14,644	16,245	0

Boundary conditions of sand, silt, clay, POM, and DOC in the water column of each segment are presented in Table S5.

Table S5 Initial concentrations of sand, silt, clay, and POM in the water column and two sediment layers

Segment Name	Sand [mg L^{-1}]	Silt [mg L^{-1}]	Clay [mg L^{-1}]	POM [mg L^{-1}]	DOC [Carbon mg L^{-1}]
WC 1	0.00	1.85	9.60	6.63	5.6
WC_2	0.00	1.80	9.57	6.59	5.6
WC 3	0.00	1.77	9.56	6.58	5.6
WC_4	0.00	1.74	9.53	6.55	5.6
WC 5	0.00	1.71	9.52	6.53	5.6
WC_6	0.00	1.68	9.50	6.51	5.6
WC 7	0.00	1.68	9.50	6.51	5.6
WC_8	0.00	1.67	9.49	6.50	5.6
WC 9	0.00	1.67	9.49	6.50	5.6
WC_10	0.00	1.66	9.48	6.49	5.6
WC 11	0.00	1.65	9.48	6.49	5.6

Segment Name	Sand [mg L^{-1}]	Silt [mg L^{-1}]	Clay [mg L^{-1}]	POM [mg L^{-1}]	DOC [Carbon mg L^{-1}]
WC_12	0.00	1.65	9.47	6.48	5.6
Reedy WC	0.00	1.71	9.51	6.53	5.6
Brushy_WC	0.00	1.76	9.55	6.57	5.6

1.2 Brier Creek Water Chemistry Conditions

For Brier Creek water, total organic carbon was analyzed with a Shimadzu TOC-5050A Total Organic Carbon Analyzer and major water ions were measured with an inductively coupled plasma spectrometer−mass spectrometer (ICP−MS, PerkinElmer ELAN 6000, Waltham, MA). Analysis results are available in Table S6.

Table S6 Water chemistry of Brier Creek[1]

	Content	Concentration (mM)
Cations (mM)	[Na^+]	0.3068 ± 0.0143[a]
	[Mg^{2+}]	0.0433 ± 0.0022
	[Al^{3+}]	BDL[b]
	[K^+]	0.0200 ± 0.0014
	[Ca^{2+}]	0.1865 ± 0.0121
	[Fe^+]	0.0065 ± 0.0006
TOC (mg/L)	Before Filtration	5.54 ± 0.13
	Filtered through 0.45 μm membrane	5.58 ± 0.13

[a] Mean and standard deviation. [b] Below detection limits.

1.3 Brier Creek Sediment Characterization

Brier Creek sediment was wet sieved, thoroughly rinsed with deionized water, oven-dried, and stored in a closed container before use. Sediment characterization was performed in the Laboratory for Environmental Analysis at the University of Georgia (Athens, GA). Total organic carbon was analyzed with a LECO CNS-2000 analyzer and particle size distribution determined using the hydrometer method. Mineralogical analyses were performed on a Brucker D8-Advanced multi-purpose X-ray diffraction system. The bulk data were collected over a range of 2 to 70° 2θ using a Co-Kα source, and the diffraction patterns were matched to the International Centre for Diffraction Data (ICDD) Powder Diffraction Files (PDF).

Table S7 Major properties of Brier Creek sediment[1]

	Brier Creek sediment		
Particle size (%)	93.9 – 95.5 sand[a]	0.2 - 0.9 silt	4.3 – 5.1 clay
Organic carbon (% by weight)	0.010 ± 0.006[b]		

pH	6.02 ± 0.05[b]
Mineralogy	quartz

[a] Range of duplicate measurements. [b] Mean and standard deviation for triplicate measurements.

2. Light attenuation and phototransformation implementation in WASP8

2.1 Acquisition of sunlight radiation intensity at Brier Creek surface

Hourly sunlight intensity at the surface of Brier Creek was retrieved and input into WASP8 This section shows how surface sunlight intensity data was acquired.

The time series data of sunlight radiation intensity (250 – 2500 nm) on the North American ground surface are available on the North America Land Data Assimilation System (NLDAS) website.

The coordinates of Brier Creek, GA are 32.7835° N and 81.4327° W, and the NLDAS cell coordinates of Brier Creek is X = 348 and Y = 62 after calculation.

After obtaining NLDAS cell coordinates, starting time and ending time of simulation needed to be specified. For this study, starting time and ending time of simulation are on 1996 January 1st, 12 am EST and on 2017 January 1st, 12 am EST, respectively. After transforming the time from EST to GMT, starting time and ending time in GMT are 1996 January 1st, 5 am and 2017 January 1st, 5 am.

Next, the URL is constructed following a specific style. NLDAS cell coordinates are written as X*longitude*-Y*latitude*, for Brier Creek, X348-Y62. For the time point at the beginning and the end of simulation, it is *year-month-date*T*time*. For this study, starting time is 1996-01-01T50 and ending time is 2017-01-01T50.

So the URL construction

https://hydro1.gesdisc.eosdis.nasa.gov/daac-bin/access/timeseries.cgi?variable=NLDAS:NLDAS_FORA0125_H.002:DSWRFsfc&location=NLDAS:X348- Y62&startDate=1996-01-01T50&endDate=2017-01-01T50&type=asc2

2.2 Division of wavelength bands by latitude

The fraction of light for each wavelength band varies depending on the site location latitude. The spectral distribution of the solar radiation was determined by using data from the National Center for Atmospheric Research TUV (Tropospheric Ultraviolet-visible Radiation) model. This was done for eight dates at different latitudes. Dates included January 15, 2107; March 20, 2017; April 15, 2017; June 21, 2017; July 15, 2017; September 22, 2017; October 15, 2017; and December 221, 2017. This included both equinoxes and solstices. The latitudes used were 0, 10, 20 30, 40, 50, and 60 degrees North. These dates and

coordinate combinations were chosen to estimate total downward spectral irradiance throughout the year, coast-to-coast in North America. Default values were used for Overhead Ozone Column (300 Dobson units), Surface Albedo (0.1) and 0 km was assumed for ground elevation. The inputs for clouds and aerosols were left unchanged, and output option 2 was selected for Spectral Irradiance (W m^{-2} nm^{-1}). For accurate comparison, only mid-day TUV values were used for each corresponding day/coordinate.

By converting the raw spectral data into segregated wavelength bins (i.e. 295-304, 305-314, etc.) we were able to update the existing WASP8 light module with more accurate irradiation data that now enables the user to estimate the effects of photo-inactivation throughout the year. The mean was calculated for each latitude for the range of dates used. The user inputs the latitude of the site, and WASP8 linearly interpolates the value. The fraction for each wavelength band does not adjust over the course of the year. The resulting table of divisions is shown in the Table S8.

Table S8 Division of wavelength bands by latitude

		Latitude						
Color	**Wavelength Band [nm]**	**0° N**	**10° N**	**20° N**	**30° N**	**40° N**	**50° N**	**60° N**
UVB med	295 – 304	0.00015	0.00015	0.00013	0.00011	0.00008	0.00006	0.00004
UVB high	305 – 314	0.00142	0.00139	0.00132	0.0012	0.00104	0.00085	0.00067
UVA low	315 – 334	0.00845	0.00839	0.00825	0.00801	0.00766	0.00721	0.00681
UVA med	335 – 354	0.01141	0.01137	0.01126	0.01108	0.01082	0.01052	0.01054
UVA high	355 – 379	0.01723	0.01718	0.01706	0.01686	0.01655	0.01619	0.0163
violet	380 – 449	0.07626	0.07617	0.07593	0.0755	0.07482	0.07394	0.07443
blue	450 – 494	0.06664	0.06663	0.06659	0.06652	0.06639	0.06616	0.06644
green	495 – 569	0.10386	0.10388	0.10394	0.10402	0.10406	0.1039	0.10285
yellow-orange	570 – 619	0.06546	0.06549	0.06556	0.06566	0.06576	0.06568	0.06422
red	620 – 749	0.14914	0.14934	0.14995	0.15106	0.15282	0.1555	0.15769

2.3 Example to calculate the average light intensity in the water column

2.3.1 Hourly average light intensity calculation

After retrieving sunlight intensity for the surface of Brier Creek (I_0) and inputting them into WASP8, WASP8 internally calculates the hourly average light intensity of each wavelength band in the water column following Eqs. (1) – (4) described in the paper.

The sunlight spectrum is divided into 11 specific wavelength bands, and the attenuation coefficients for water background, [DOC], [SS], and the energy fraction of each wavelength band at 30°N are displayed

in Table 1. Even though the energy from infrared light accounts for 50% of total sunlight radiation, it is not photochemically active. We therefore ignore the contribution of infrared light to average light intensity; for the rest of this paper, we only consider average light intensity contributed from ultraviolet and visible light groups, which total 10 wavelength bands. [SS] in the river are invariable in each segment over 20 years simulation period due to the constant flow, and we assume [DOC] is a constant at 8 mg L^{-1} in Brier Creek. Therefore, the diffuse attenuation coefficient for each wavelength band is invariable in each segment over the 20-year simulation. Each segment has 10 diffuse attentuation coefficients, and the river of interest is divided into 12 segments, so there are totally 12 x 10 values of diffuse attentuation coefficients in the water column as shown in Table 14.

Year 2016 was selected to illustrate the calculation process. Year 2016 has 366 days, and thus has 8784 hours, resulting in 8784 I_0. In each river segment, each wavelength band has 8784 average light intensity values in 2016, and 10 wavelengths have 8784 x 10 values of the average light intensity in the water column. WASP8 internally calculate these. We selected the first day of 2016 as an example to show the calculation process for the red band in stream segment 1.

Sunlight radiation intensities at the surface of Brier Creek are shown in Table S9. Based on Eq. (1), the diffuse attenuation coefficient of the red band is in Table S7. Then Eq.(2) is used to calculate the light intensity at the bottom of water column. In the Eq.(2), K_e and k_{band} of red and water depth (z) are constant, which are 8.8310 m^{-1}, 0.15217 and 1.73 m, respectively. I_0 is the only variable parameter by hours. Results I_z of red band on the first day of 2016 are displayed in Table S9. After each I_z is ready, Eq.(3) is used to calculate the average light intensity in the water column.

Table S9 Sunlight radiation intensity at the water surface, diffuse attenuation coefficient, water depth, energy fraction, and the hourly average light intensity of red wavelength band in the water column.

Time on 1/1/1996, EST	Surface sunlight radiation intensity, I_0 (W m^{-2})	Diffuse attentuation coefficient of red band, K_e (m^{-1})	Water column depth, z (m)	Energy fraction of red band at 30 °N, k_{band}	Hourly calculated light intensity at the bottom of water column, I_z (W m^{-2})	Hourly calculated average light intensity in the water column, I_{av} (W m^{-2})
0	0.00	8.8310	1.73	0.15217	0	0
1	0.00	8.8310	1.73	0.15217	0	0
2	0.00	8.8310	1.73	0.15217	0	0
3	0.00	8.8310	1.73	0.15217	0	0
4	0.00	8.8310	1.73	0.15217	0	0
5	0.00	8.8310	1.73	0.15217	0	0
6	0.00	8.8310	1.73	0.15217	0	0
7	0.00	8.8310	1.73	0.15217	0	0

8	16.80	8.8310	1.73	0.15217	5.92E-07	0.1673
9	50.20	8.8310	1.73	0.15217	1.77E-06	0.5000
10	69.10	8.8310	1.73	0.15217	2.44E-06	0.6883
11	89.10	8.8310	1.73	0.15217	3.14E-06	0.8875
12	101.00	8.8310	1.73	0.15217	3.56E-06	1.0060
13	165.00	8.8310	1.73	0.15217	5.82E-06	1.6435
14	148.00	8.8310	1.73	0.15217	5.22E-06	1.4741
15	121.00	8.8310	1.73	0.15217	4.27E-06	1.2052
16	56.90	8.8310	1.73	0.15217	2.01E-06	0.5667
17	17.70	8.8310	1.73	0.15217	6.24E-07	0.1763
18	0.00	8.8310	1.73	0.15217	0	0
19	0.00	8.8310	1.73	0.15217	0	0
20	0.00	8.8310	1.73	0.15217	0	0
21	0.00	8.8310	1.73	0.15217	0	0
22	0.00	8.8310	1.73	0.15217	0	0
23	0.00	8.8310	1.73	0.15217	0	0

2.3.2 Daily average light intensity calculation

Sunlight radiation intensity data at the surface of Brier Creek is recorded in units of W m^{-2} and hourly average light intensity is calculated by WASP8. In order to calculate daily average light intensity, the trapezoid rule is used to calculate the daily average light intensity in the water column.

The calculated results of hourly average light intensity of red band in segment 1 on the first day of 2016 are listed in Table S9. Trapezoid rule formula is expressed as

$$I_{day,\ \lambda} = \sum_{i=1}^{n=23} \left(I_{i,\lambda} + I_{i+1,\lambda}\right) \times \Delta h \times \frac{1}{2}$$

where I_i and I_{i+1} (W m^{-2}) are the hourly average light intensities in the water column at consecutive time points in a day, Δh is the time interval (1 hour), and I_{day} (W m^{-2}) is the daily average light intensity in the water column. The plot of hourly average light intensity of the red band in the water column as a function of time on the first day of 2016 is shown in Fig. S1, which visualizes the calculation process.

The calculation of total monthly daily average light intensity in the water column is the sum of the daily average light intensity in the water column, which is presented in Fig. S2.

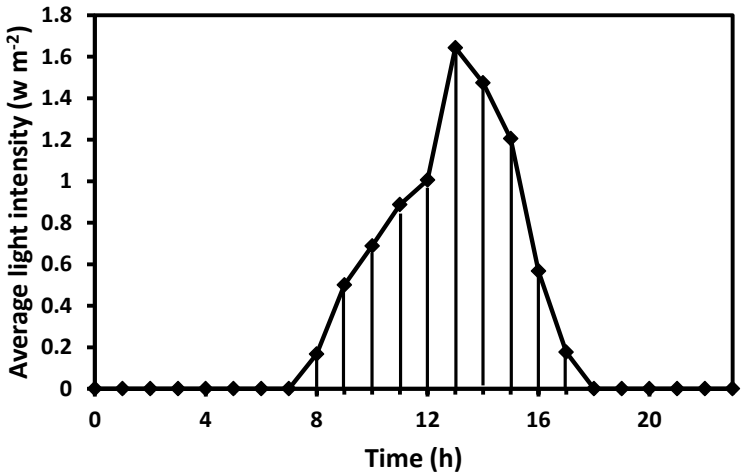

Fig. S1 The hourly average light intensity in the water column in the stream segment 1 on the first day of 2016

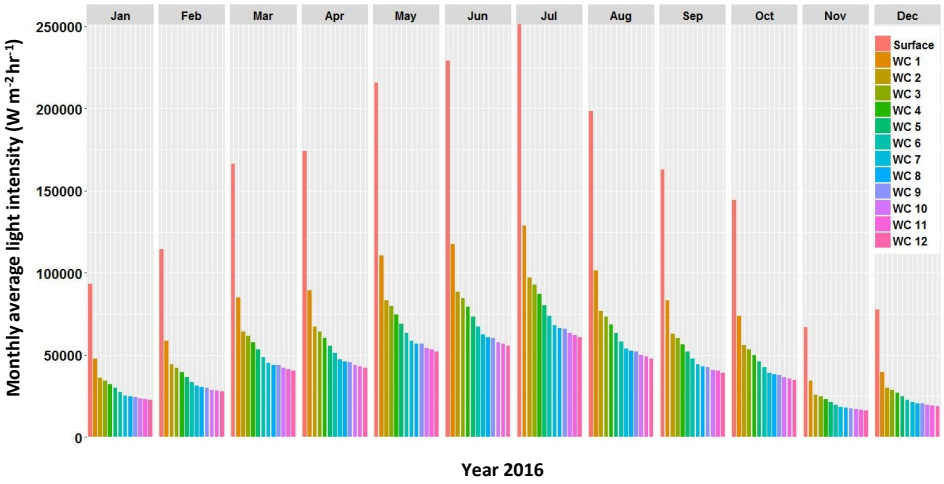

Fig. S2 Monthly light intensity in the water column in 12 stream segments in 2016. 'Surface' represents sunlight radiation intensity at the river surface; WC represents the monthly average light intensity in the water column.

2.4 GO Phototransformation Model

Table S10 Measured GO wavelength-dependent phototransformation reaction rate of each wavelength band

Wavelength band partitioning	$\frac{k_{obs}^{n}}{I^{n}}$ (d^{-1} W^{-1} m^{2})
620 - 749 nm (red)	0.001055
570 - 619 nm (yellow-orange)	0.001521
495 - 569 nm (green)	0.002097
450 - 494 nm (blue)	0.002912
380 - 449 nm (violet)	0.006566
355 - 379 nm (uVa high)	0.005725
335 - 354 nm (uVa medium)	0.006476
315 - 334 nm (uVa low)	0.007209
305 - 314 nm (uVb high)	0.007694
295 - 304 nm (uVb medium)	0.007898

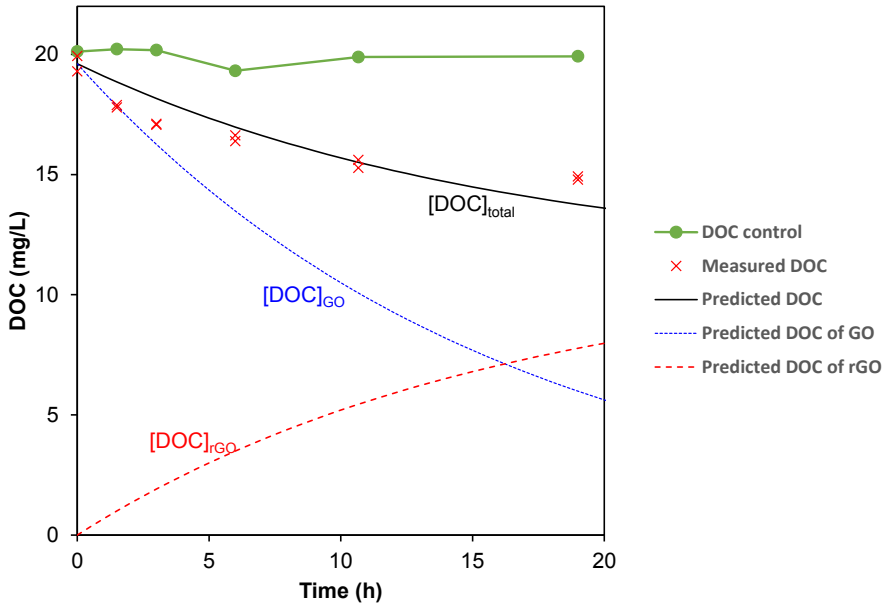

Fig. S3 Measured and predicted temporal trends of DOC of 40 mg L^{-1} GO suspension under exposure to solar light irradiation. DOC control run is conducted by exposing GO in the dark without simulated sunlight radiation.

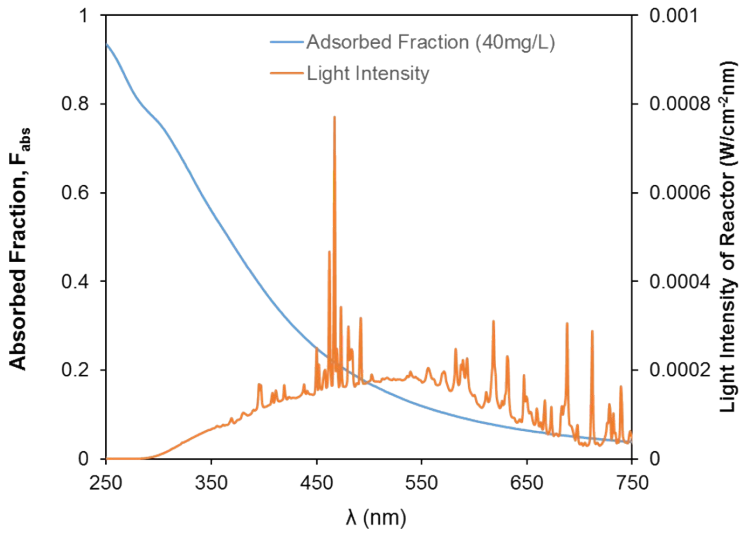

Fig. S4 Light adsorbed fraction by GO (40 mg/L) and the intensity spectrum of solar light simulator

3. GO and rGO stability study in Brier Creek

3.1 Materials and Methods

3.1.1 Synthesis and Characterization of GO and rGO

GO was synthesized using a modified Hummers method described previously;[4] solvothermal reduction of GO to produce reduced GO (rGO) was achieved by heating a GO suspension in N-Methyl-2-pyrrolidone (NMP) to 150°C while constantly stirring in a silicone oil bath for 2 hours.[5] After solvothermal reduction, the rGO was separated from the NMP using vacuum filtration with 0.1µm alumina filters (Millipore), rinsed heavily with DI water, and re-dispersed in DI water to form a working stock suspension at an approximate concentration of 1 mg/mL. GO and rGO atomic force microscopy (AFM) images were collected using published procedures [6] are presented in Figure S5. The relative concentration of GO and rGO functional groups were determined by X-ray photoelectron spectroscopy (XPS) and are presented in previous studies.[5, 7]

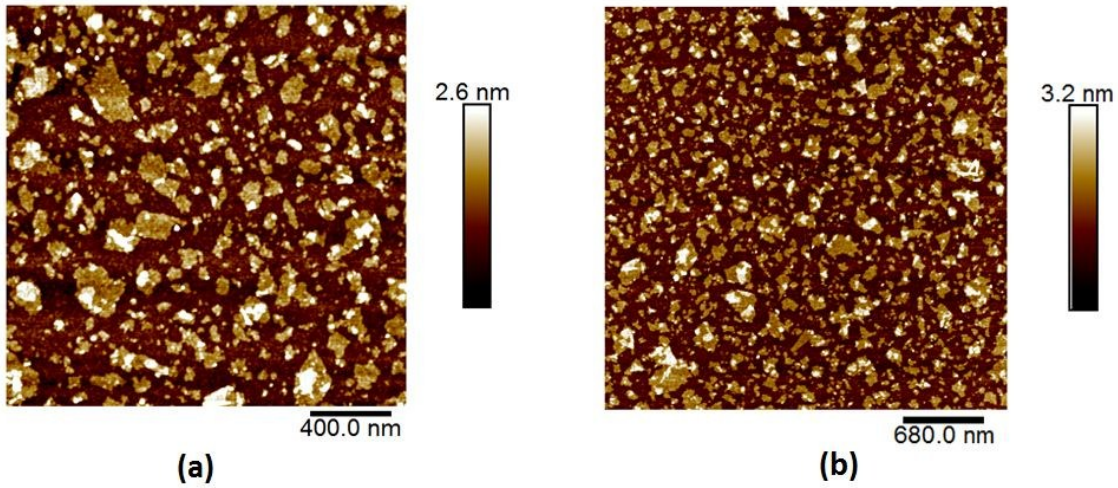

Fig. S5 AFM of GO and rGO.

3.1.2 WASP8 Parameterization with Heteroaggregation Attachment Efficiencies (α_{het}).

Sediment from Brier Creek, a coastal plain river that is part of the Savannah River drainage basin, was collected, wet sieved, and the 125-250 μm size fraction utilized for the GO and rGO heteroaggregation studies. Particle size distribution, mineralogical composition and organic carbon content of the Brier Creek sediment have been reported.[1] Brier Creek water has also been analyzed for major naturally occurring ions by ICP-MS, for particulate organic matter (POM, suspended organic materials retained on 0.45 filter), and DOC content.[1]

GO and rGO were dispersed in Brier Creek water samples via ultrasonication with a probe sonicator (Sonic & Materials, Newton, CT) in an ice-water bath for 3 min at an average energy level of ~32 Watts and GO and rGO concentration in the supernatant determined using UV-vis absorbance at 500 nm (Enspire Multimode Reader 2300, PerkinElmer, MA) and pre-determined calibration curves. Electrophoretic mobility (EPM) was determined using phase analysis light scattering, and the intensity-averaged (Z-average) hydrodynamic diameter (Dh) and polydispersity index (PDI) were determined using dynamic light scattering [DLS, Nano ZetaSizer (Malvern Instruments, Worcestershire, U.K.)] (4). Instrument performance for Dh and EPM measurements were verified using NIST-traceable polystyrene nanosphere standards (Thermo-Fisher, Fremont, CA) and a ζ-potential transfer standard (Malvern Instruments, Worcestershire, U.K.), respectively.

Table S11 Physicochemical properties of GO and rGO suspended in Brier Creek water.

	D_h (nm)	PDI	EPM (10^{-8} m^2 V^{-1} s^{-1})
GO	508.9 ± 2.7	0.49 ± 0.05	-5.25 ± 0.06
rGO	689.3 ± 17.3	0.27 ± 0.09	-3.69 ± 0.19

Table S12 Physicochemical properties, deposition rate, and resuspension rate of rGO-SS.

Solid Type	WASP Particle Diameter [mm]	Settling Velocity [m d^{-1}]	Deposition Rate [m d^{-1}]	Resuspension Rate [m d^{-1}]	Density [g cm^{-3}]
GO	508.9E-06	0	0	0	2.1
rGO	689.3E-06	0	0	0	2.0
rGO-Silt	0.006	2.80	1.40	2.0E-05	2.65
rGO-Clay	0.002	0.32	0.16	2.0E-05	2.65
rGO-POM	0.005	0.50	0.25	2.0E-05	1.5

Kinetics of GO and rGO heteroaggregation with Brier Creek particulates were measured in batch systems as described in prior studies. [1, 8] Briefly, GO and rGO dispersed in Brier Creek water were placed in glass vials with Brier Creek sediment and the decrease in GO or rGO concentration in the supernatant monitored over time. To account for the potential confounding effects of homoaggregation and subsequent aggregate precipitation on heteroaggregation determination, Dh was monitored in all samples for the duration of the experimental period.

The heteroaggregation attachment efficiency (α_{het}) for GO, rGO and Brier Creek particulates is estimated:

$$\alpha_{het} = \frac{k_{het}}{k_{coll} C_{particle}^{SPM}}$$

where k_{het} is the experimentally measured heteroaggregation rate constant, k_{coll} is the GO, rGO -particle collision rate, and $C_{particle}^{SPM}$ is the concentration of suspended particles. The GO, rGO-SPM heteroaggregation rate may be estimated by measuring GO, rGO concentration decrease over time as heteroaggregation with SPM proceeds, and then using the slope of ln GO, rGO concentration vs time plots to determine the first-order rate constant, k_{het}. In this study, k_{het} is measured for one particle size fraction (125-250 μm size fraction of Brier Creek sediment) yielding an α_{het} value for all particulate surfaces, and k_{coll} values are calculated for each different SPM size class as described in prior studies (5-7).[8, 9]

3.2 RESULTS AND DISCUSSION

Table S11 and S12 contains the key physicochemical parameters of the GO and rGO suspensions used in this study. The rGO D_h is somewhat larger than that of GO, which is consistent with measurements made on similar materials in a prior study where D_h was observed to increase with degree of GO reduction (2). Both materials are negatively charged when dispersed in water. This negative charge, which arises from dissociation of a proton from the oxygen containing functional groups of GO and rGO (4), results in stable suspensions where no homoaggregation of GO or rGO is observed over a 14-day period (Fig. S6). Previous studies have shown that GO is highly stable in both natural surface waters and synthetic surface waters with negligible homoaggregation, mainly due to the specific physiochemical properties of GO. GO sheets surface is enriched with carboxyl, hydroxyl, and epoxy groups, leading to that GO surface is strongly negatively charged as well as characterized with hydrophilic surface.[7, 10-12] It is commonly acknowledged that negatively charged colloids with zeta potential less than -30 mV are regarded to be electrostatically stable [10], and reported zeta potential of GO ranged between -50 mV and -40 mV.[13, 14] Therefore, electrostatic repulsion is the primary driving force to prevent GO from homoaggregating.[15] Also, studies show that homoaggregation can happen only under high ionic strength condition, and GO can remain stable over a wide range of pH from 4 to 14.[7]

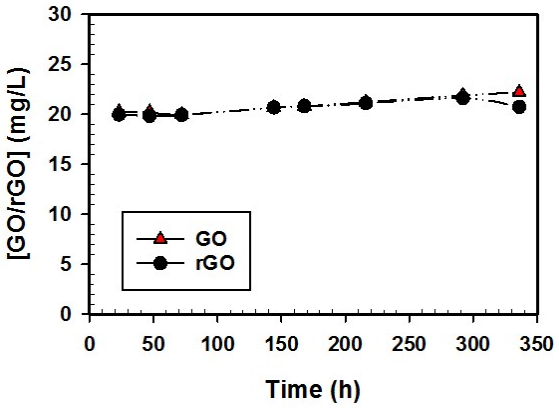

Fig. S6 Homoaggregation of GO and rGO in Brier Creek water.

There is no measurable GO heteroaggregation with Brier Creek sediment, likely due to GO's high negative charge and the predominant negative charge of sediments that arises from the dissociation of the weak acid groups of natural organic matter coating sediments. Another possible reason could be that the interaction of GO between mineral particles is weakened by the formation of hydrogen bonds between water molecule and GO surface.[16] Again, possible attachment of natural organic matter to GO surface can also stabilize GO and prevent GO from being attached to suspended solids.

Being less negatively charged and having a lower O/C ratio than GO (0.3 vs 0.5), measurable heteroaggregation of rGO was observed (Fig. S7). rGO heteroaggregation with Brier Creek sediment was first-order (average $r^2 = 0.95$) with respect to rGO concentration (Fig. S7) yielding a k_{het} value of 0.0116 day^{-1}. This k_{het} value may be substituted in equation 1 with calculated k_{coll} values to yield an α_{het} value of 2.045×10^{-7}, which represents the fraction of rGO-SPM collisions that result in attachment. Since α_{het} is concentration independent and unitless, it is a very useful parameter for quantifying rGO-SPM interactions.

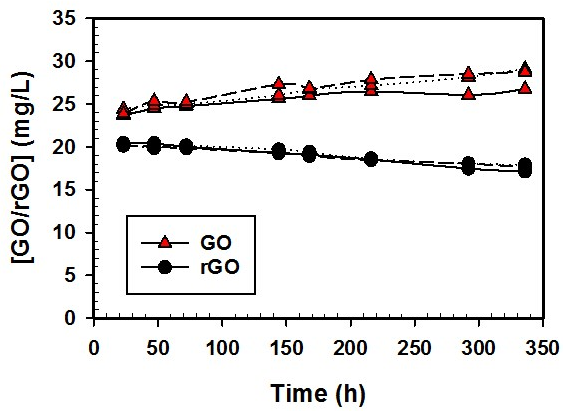

Fig. S7 Heteroaggregation of GO/rGO with Brier Creek sediment.

4. rGO-SS concentration in sediment

Simulation result indicates that a linear increase of rGO-SS in each sediment layer when heteroaggregation attachment coefficients in water column increase. Its equation is expressed as

$$[rGO-SS]_n = [rGO-SS]_0 \frac{\alpha_n}{\alpha_0}$$

where $[rGO\text{-}SS]_n$ is total rGO-SS concentration (including rGO-silt, rGO-clay, and rGO-POM) in the two sediment layers at an assigned heteroaggregation coefficient at a given time, $[rGO\text{-}SS]_0$ is rGO-SS concentration when heteroaggregation attachment coefficient is at 2×10^{-7} at a given time. The α_0 is 2×10^{-7}, and α_n is the assigned heteroaggregation rate. Simulation results also suggest that this linear increase is effective when α ranges between 2×10^{-7} and 2×10^{-2}.

5. GO mass flowrate analysis

The principle of contaminant mass flowrate analysis in a river is illustrated in the following figure

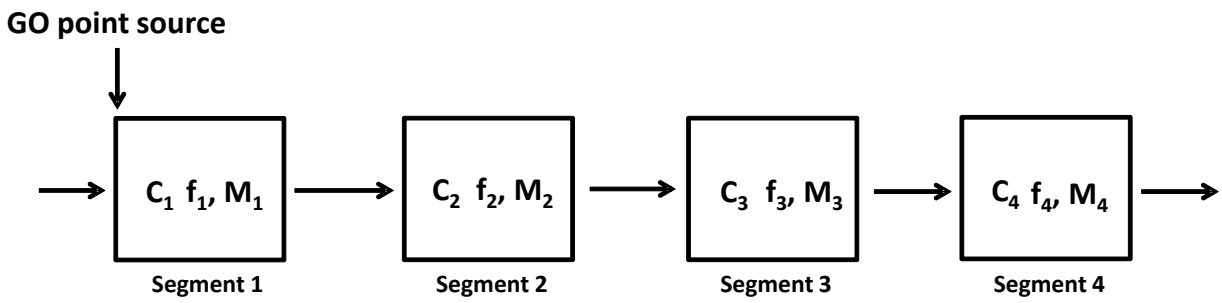

Figure S8. Illustration of GO mass flowrate in each segment in the river

Mass flowrate in each segment in Brier Creek can be expressed as

$$M_i = f_i C_i \quad (i \text{ is segment number},\ 1 \le i \le 12) \qquad \text{(S1)}$$

where M_i is the GO mass flowrate in each segment (ng s^{-1}); f_i is the outflow rate in each segment, and outflow rate has counted the flow from tributary coming into each segment (m s^{-3}); C_i is the mean [GO] in each segment. When $i = 0$, M_0 is the initial condition and is the location where GO constantly loads into the river as 0.1 kg d^{-1}, and it is equal to 1157407 ng s^{-1}. In WASP8, f_i and C_i can be internally calculated based on WASP input data.

If neither chemical reaction nor heteroaggregation happens to GO in the river, M_i in each segment is a constant and is equal to M_0

$$M_0 = M_i \quad (1 \le i \le 12) \qquad \text{(S2)}$$

If GO undergoes phototransformation, M_i will drop compared to M_0. The GO phototransformation rate in each segment is calculated by

$$GO\ Phototransformation\ Rate\ (\%) = \frac{M_0 - M_i}{M_0} \times 100 \qquad \text{(S3)}$$

The mass flowrate analysis results in each segment are shown in the following figure.

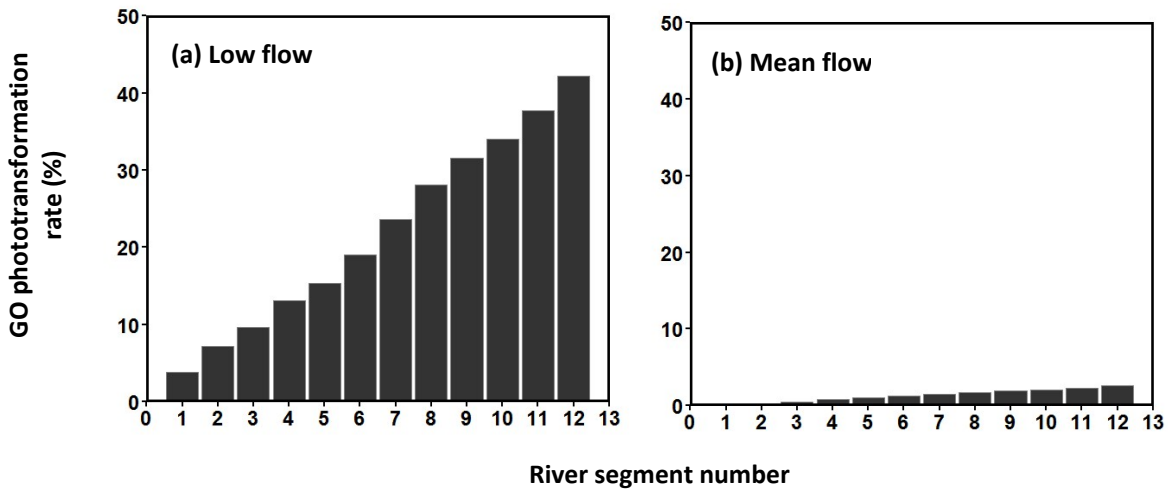

Fig.S9 (a) and (b) show the GO phototransformation rate in each segment under two flow conditions

At the mean flow condition, the phototransformation rate of GO in each segment is presented in Fig. S9 (b), and a maximum GO transformation rate is approximately 2.5% in the 12th segment. Based on this analysis, the decrease of [GO] along the river is due mainly to hydrologic effect, or due to dilution effect. At the low flow condition in Brier Creek, phototransformation has a substantial effect on the decrease of [GO] in Brier Creek. As can be seen from the simulation results presented in Fig. S9 (a), more than 10% of GO phototransformation occurs 3rd segment, and more than 40% of GO undergoes phototransformation in the last segment. These simulations indicate that at the low flow condition, phototransformation cannot be ignored and a considerable amount of GO will transformed into rGO. Mean flow condition represents the general flow condition in Brier Creek, but low flow condition applies to the situation when droughts happen, such as in 1998-2000, 2008, 2012, and 2015 in Georgia, USA. From the ecological risk point of view, our analysis also suggested that even though under mean flow condition phototransformation does not have a large effect on [GO] in each segment, rGO removed by heteroaggregation can accumulate in the sediment layers appreciably, which takes 100 years to remove. rGO in the sediment could be a long-term threat to the creatures in the water column and sediments.

6. Heteroaggregation model

The equation to calculate the heteroaggregation rate constant (k_{hetagg}, s^{-1}) in a certain segment is

$$k_{hetagg} = \alpha_{hetagg} \left(\sum_{n=1}^{3} k_{coll,n} c_{ss,n,i} \right) \quad \text{(S4)}$$

for n: $1 \le n \le 3$ (number of suspended solids)

for i: $1 \le i \le 12$ (number of segment number)

where α_{hetagg} is the heteroaggregation attachment efficiency measured in the laboratory; $k_{coll,n}$ is the collision rate of NM to a specific type of suspended solid ($m^3\ s^{-1}$), and in this study it is rGO to a suspended solid; $c_{ss,n.i}$ is particle concentration of a specific type of suspended solid in a segment (particle number in m^{-3}).

The following equation corresponds to the collision rate $k_{coll,n}$

$$k_{coll,n} = \frac{2k_B T_{water}(r_{rGO} + r_{solid,n})^3}{3\mu_{water} r_{rGO} r_{solid,n}} + \frac{4}{3} G(r_{rGO} + r_{solid,n})^3 + \pi(r_{rGO} + r_{solid,n})^3 \left| v_{rGO} - v_{solid,n} \right| \quad \text{(S5)}$$

where r_{rGO} is hydrodynamic radius of rGO and $r_{solid,n}$ are radius suspended solids (m), respectively. v_{rGO} and $v_{solod,n}$ are settling velocity of rGO and suspended solids ($m^3\ s^{-1}$). In WASP8, we assume free NMs do not settle due their colloidal properties, so v_{rGO} is 0. All other terms in the Eq.S5 are presented in Table S13, and besides water temperature all other constants are internally implemented in WASP8.

Table S13 Parameter constant values in Equation S4

Parameters	Symbol	Values	Unit
Boltzmann constant	k_B	1.38×10^{-23}	$J\ K^{-1}$
Water temperature	T_{water}	15	◦C
Dynamic viscosity of water	μ_{water}	1.002	mPa s
Shear rate	G	10	s^{-1}

$k_{river,i}$ is the river flow constant (s^{-1}) in each segment can be expressed as

$$k_{river,i} = \frac{f_i}{V_i} \quad \text{(S6)}$$

where $f_{,i}$ is the outflow rate of each segment ($m^3\ s^{-1}$) that can be internally calculated by WASP8; V_i is the water volume in each segment (m^3).

The equation to calculate NM particle concentration is

$$[Particle_{NM}] = \frac{(10^{-12})[NM]}{\rho_{NM} V_{NM}} = \frac{(10^{-12})[NM]}{\rho_{NM}\left[\frac{4}{3}\pi(\frac{d_{NM}}{2})^3\right]} \quad \text{(S7)}$$

where [$Particle_{NM}$] is NM particle concentration (particle number in L^{-1}); [NM] is NM mass concentration (ng L^{-1}); ρ_{NM} is NM density (kg m^{-3}); d_{NM} is NM hydrodynamic diameter (m).

The detailed computational processes of WASP8 NM module are: (1) WASP interface receives inputs in mass; (2) WASP internally converts mass concentrations of NMs and suspended solids into particle number based on the mass concentration that users input into WASP8; (3) WASP8 calculates NM particle number; (4) WASP converts particle number concentrations to mass concentrations when calculation is done; and (5) WASP outputs mass concentration to users.

5. Other figures and tables

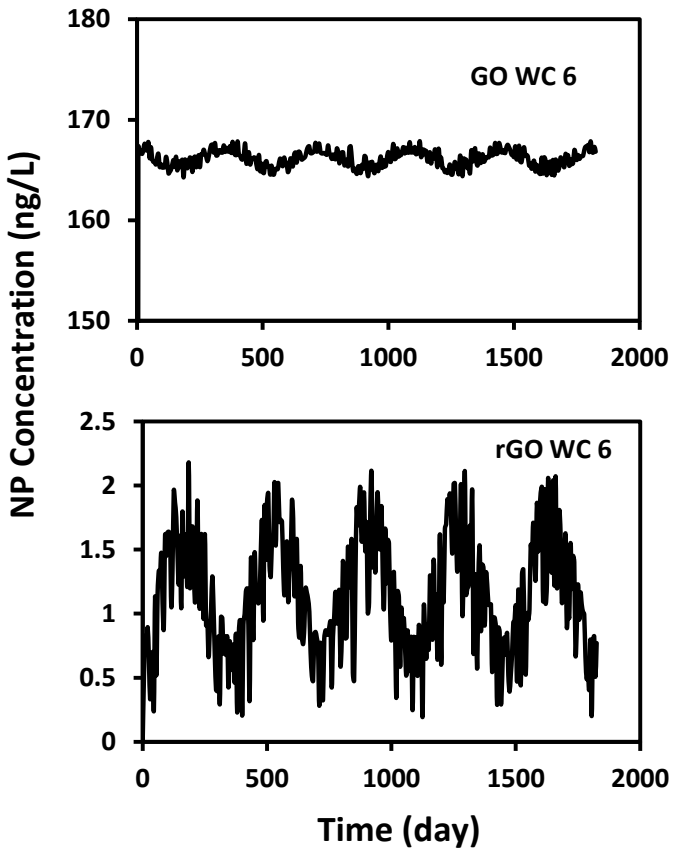

Fig. S10 Free [GO] and [rGO] in the water column in stream segment 6 from 1997 to 2001 at mean flow condition.

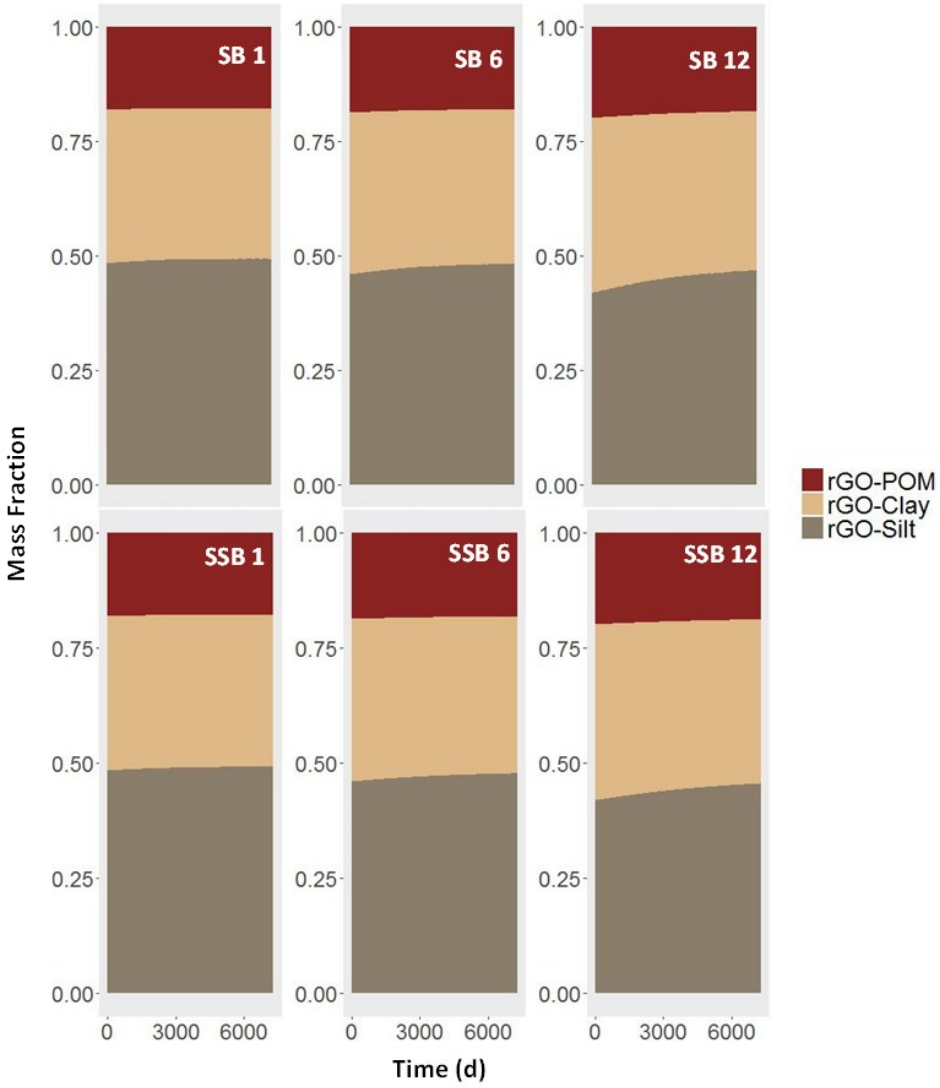

Fig. S11 rGO-SS mass fractions in two sediment layers at the mean flow condition. Mass fraction is calculated that each rGO-SS mass is divided by the sum of three kinds of rGO-SS mass together. SB represents surface sediment, and SSB represents subsurface sediment.

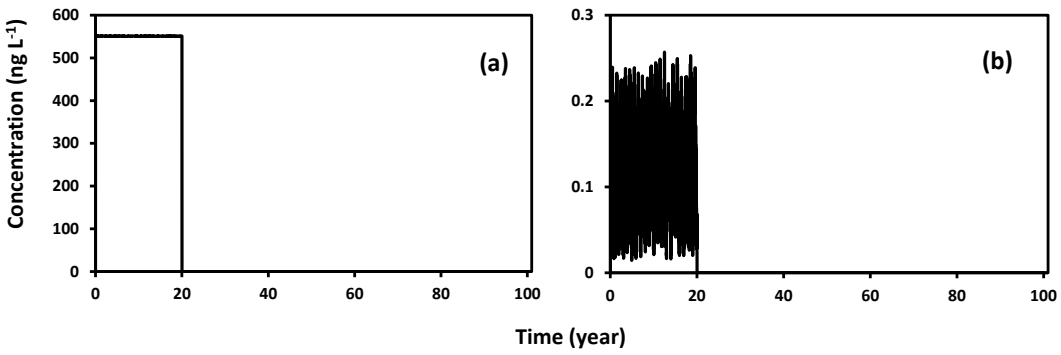

Fig. S12 Free GO and rGO recovery simulation results in the water column in stream segment 1at the mean low condition. (a) Free GO, and (b) free rGO

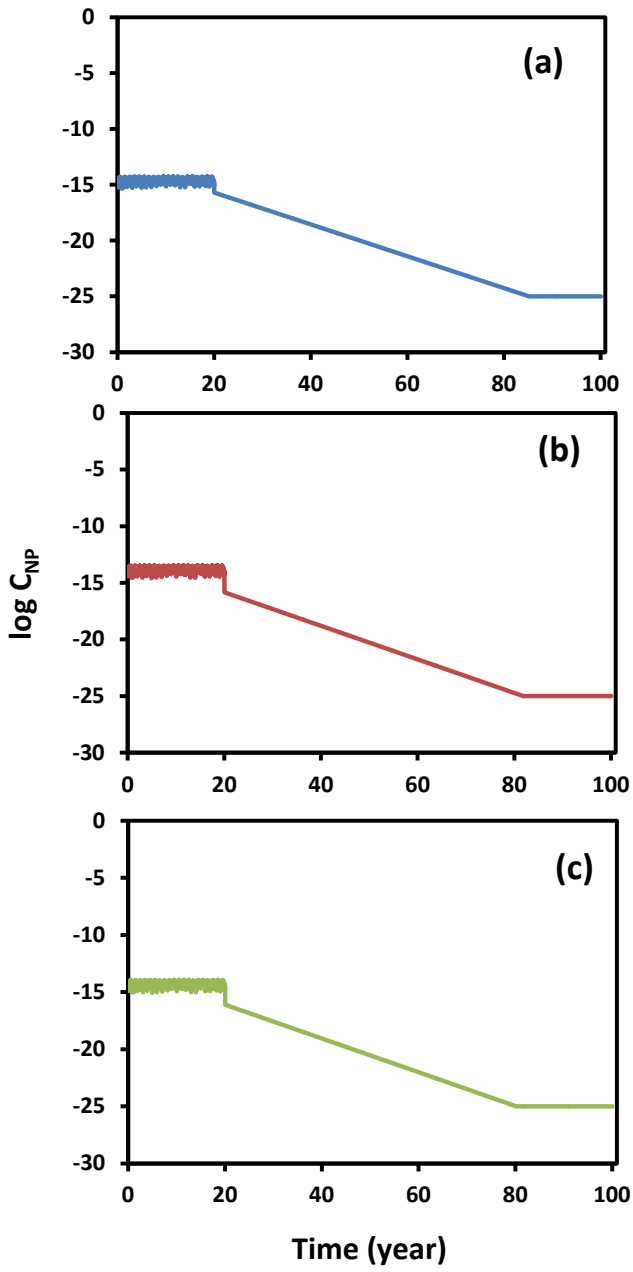

Fig. S13 rGO-SS recovery simulation results in the water column in stream segment 1at the mean flow condition. (a) rGO-silt, (b) rGO-clay, and (c) rGO-POM. C_{NP} represents rGO-SS concentration (ng L^{-1}) in the water column. Due to rGO-SS concentration in the water column is extremely low, so log scale expression is used to indicate rGO-SS concentration in the water column.

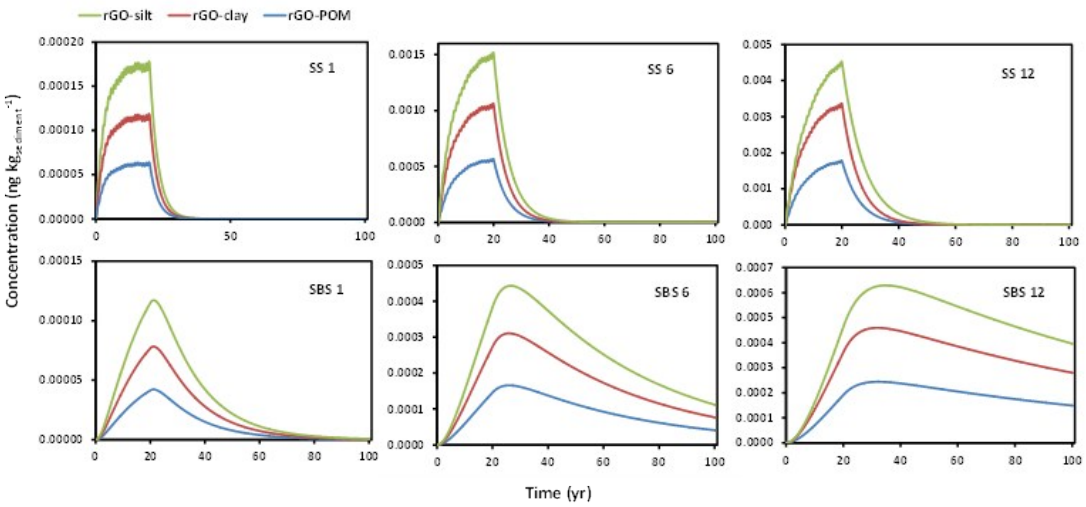

Fig. S14 rGO-SS recovery simulation results in sediments in segment 1, 6 and 12 at the mean flow condition. SB refers to surface sediment, SSB refers to subsurface sediment.

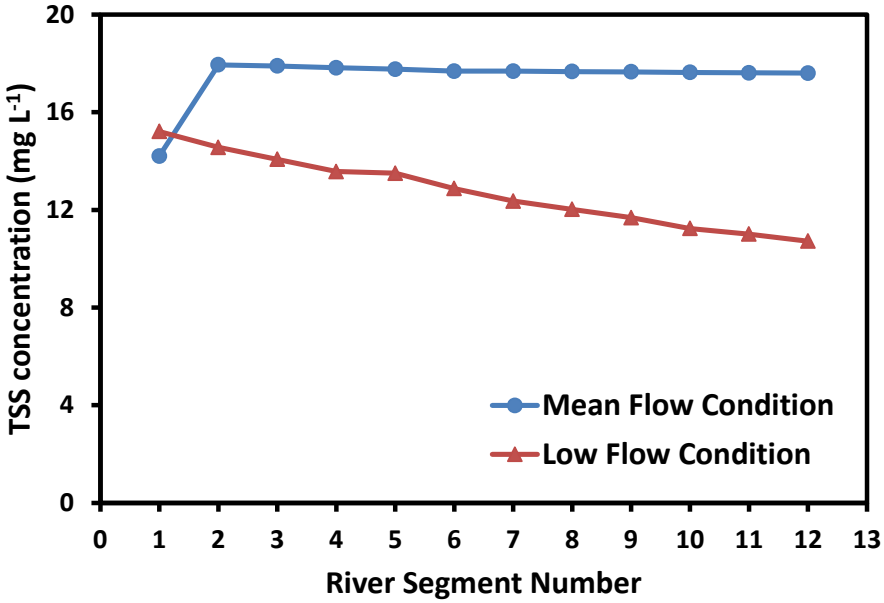

Fig.S15 TSS concentrations at steady state in each segment for both flow conditions.

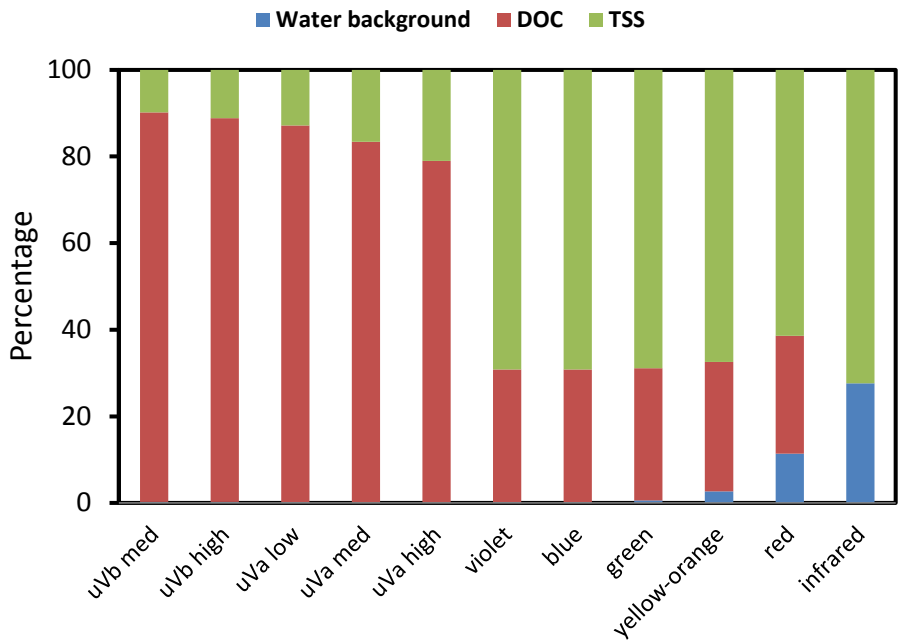

Fig.S16 Percentage of contributions of water background attenuation, DOC attenuation and suspended solids attenuation to the diffuse attenuation coefficient of each wavelength band in segment 1.

Table S14 GO and rGO statistical analysis of each year from 1997 to 2016 in stream segment 1

	GO results					rGO results				
Year	Mean [GO] (ng L^{-1})	Max [GO] (ng L^{-1})	Min [GO] (ng L^{-1})	85% quantile [GO] (ng L^{-1})	15% quantile [GO] (ng L^{-1})	Mean [rGO] (ng L^{-1})	Max [rGO] (ng L^{-1})	Min [rGO] (ng L^{-1})	85% quantile [rGO] (ng L^{-1})	15% quantile [rGO] (ng L^{-1})
1997	550.9421	551.1167	550.7114	551.0440	550.8388	0.1124	0.2393	0.0164	0.1692	0.0563
1998	550.9385	551.1143	550.7239	551.0382	550.8231	0.1144	0.2324	0.0177	0.1778	0.0595
1999	550.9368	551.1094	550.7383	551.0294	550.8375	0.1153	0.2245	0.0204	0.1699	0.0644
2000	550.9363	551.1159	550.7139	551.0257	550.8236	0.1156	0.2379	0.0168	0.1776	0.0664
2001	550.9407	551.1204	550.7162	551.0450	550.8522	0.1131	0.2366	0.0143	0.1619	0.0558
2002	550.9400	551.1161	550.7123	551.0376	550.8366	0.1136	0.2388	0.0167	0.1704	0.0599
2003	550.9439	551.1025	550.7236	551.0277	550.8401	0.1114	0.2326	0.0242	0.1685	0.0653
2004	550.9333	551.1126	550.7298	551.0297	550.8483	0.1172	0.2292	0.0186	0.1640	0.0642
2005	550.9308	551.1025	550.7342	551.0373	550.8307	0.1186	0.2268	0.0242	0.1737	0.0601
2006	550.9239	551.0976	550.7086	551.0226	550.8182	0.1224	0.2408	0.0269	0.1805	0.0681
2007	550.9243	551.1082	550.7016	551.0211	550.8224	0.1222	0.2447	0.0210	0.1782	0.0689
2008	550.9257	551.0910	550.6940	551.0467	550.7941	0.1214	0.2489	0.0305	0.1925	0.0573
2009	550.9397	551.1166	550.6793	551.0300	550.8473	0.1137	0.2569	0.0164	0.1645	0.0641
2010	550.9249	551.1174	550.7459	551.0206	550.8314	0.1219	0.2203	0.0160	0.1733	0.0692
2011	550.9177	551.1070	550.7056	551.0236	550.8115	0.1258	0.2425	0.0217	0.1842	0.0676
2012	550.9333	550.6929	550.6929	551.0369	550.8120	0.1173	0.0200	0.0200	0.1835	0.0600
2013	550.9343	551.1104	550.7324	551.0389	550.8333	0.1167	0.2277	0.0199	0.1722	0.0592
2014	550.9311	551.0947	550.7314	551.0390	550.8090	0.1184	0.2283	0.0285	0.1856	0.0591
2015	550.9183	551.0996	550.6867	551.0504	550.7831	0.1255	0.2529	0.0258	0.1998	0.0528
2016	550.9158	551.1100	550.7123	551.0159	550.7886	0.1269	0.2388	0.0201	0.1968	0.0718

Table S15 Diffuse attenuation coefficient (m-1) values of each specific wavelength along the whole river at mean flow conditions

	Ultraviolet light					Visible light				
Stream segment No.	UVb medium	UVb high	UVa low	UVa medium	UVa high	Violet	Blue	Green	Yellow-orange	Red
1	55.335	48.733	42.225	32.675	25.778	7.841	7.841	7.871	8.041	8.831
2	55.299	48.697	42.189	32.639	25.742	7.805	7.805	7.835	8.005	8.795
3	55.284	48.682	42.174	32.624	25.727	7.790	7.790	7.820	7.990	8.780
4	55.257	48.655	42.147	32.597	25.700	7.763	7.763	7.793	7.963	8.753
5	55.239	48.637	42.129	32.579	25.682	7.745	7.745	7.775	7.945	8.735
6	55.218	48.616	42.108	32.558	25.661	7.724	7.724	7.754	7.924	8.714
7	55.218	48.616	42.108	32.558	25.661	7.724	7.724	7.754	7.924	8.714
8	55.209	48.607	42.099	32.549	25.652	7.715	7.715	7.745	7.915	8.705
9	55.209	48.607	42.099	32.549	25.652	7.715	7.715	7.745	7.915	8.705
10	55.200	48.598	42.090	32.540	25.643	7.706	7.706	7.736	7.906	8.696
11	55.197	48.595	42.087	32.537	25.640	7.703	7.703	7.733	7.903	8.693
12	55.191	48.589	42.081	32.531	25.634	7.697	7.697	7.727	7.897	8.687

Table S16 Diffuse attenuation coefficient (m-1) values of each specific wavelength along the whole river at low flow conditions

	Ultraviolet light					Visible light				
Stream segment No.	UVb medium	UVb high	UVa low	UVa medium	UVa high	Violet	Blue	Green	Yellow-orange	Red
1	39.546	34.912	30.348	23.654	18.821	6.260	6.260	6.290	6.460	7.250
2	39.351	34.717	30.153	23.459	18.626	6.065	6.065	6.095	6.265	7.055
3	39.204	34.570	30.006	23.312	18.479	5.918	5.918	5.948	6.118	6.908
4	39.054	34.420	29.856	23.162	18.329	5.768	5.768	5.798	5.968	6.758
5	39.033	34.399	29.835	23.141	18.308	5.747	5.747	5.777	5.947	6.737
6	38.844	34.210	29.646	22.952	18.119	5.558	5.558	5.588	5.758	6.548
7	38.691	34.057	29.493	22.799	17.966	5.405	5.405	5.435	5.605	6.395
8	38.589	33.955	29.391	22.697	17.864	5.303	5.303	5.333	5.503	6.293
9	38.487	33.853	29.289	22.595	17.762	5.201	5.201	5.231	5.401	6.191
10	38.364	33.730	29.166	22.472	17.639	5.078	5.078	5.108	5.278	6.068
11	38.286	33.652	29.088	22.394	17.561	5.000	5.000	5.030	5.200	5.990
12	38.199	33.565	29.001	22.307	17.474	4.913	4.913	4.943	5.113	5.903

References

1. D. C. Bouchard, C. D. Knightes, X. Chang and B. Avant, Simulating Multiwalled Carbon Nanotube Transport in Surface Water Systems Using the Water Quality Analysis Simulation Program (WASP), *Environmental Science & Technology*, 2017.
2. T. M. F. Tissue and O. River, TOTAL MAXIMUM DAILY LOAD (TMDL).
3. K. Fuwa and B. L. Valle, The Physical Basis of Analytical Atomic Absorption Spectrometry. The Pertinence of the Beer-Lambert Law, *Analytical Chemistry*, 1963, **35**, 942-946.
4. Z. Bo, X. Shuai, S. Mao, H. Yang, J. Qian, J. Chen, J. Yan and K. Cen, Green preparation of reduced graphene oxide for sensing and energy storage applications, *Scientific reports*, 2014, **4**.
5. I. Chowdhury, N. D. Mansukhani, L. M. Guiney, M. C. Hersam and D. Bouchard, Aggregation and stability of reduced graphene oxide: complex roles of divalent cations, pH, and natural organic matter, *Environmental science & technology*, 2015, **49**, 10886-10893.
6. M. C. Duch, G. R. S. Budinger, Y. T. Liang, S. Soberanes, D. Urich, S. E. Chiarella, L. A. Campochiaro, A. Gonzalez, N. S. Chandel and M. C. Hersam, Minimizing oxidation and stable nanoscale dispersion improves the biocompatibility of graphene in the lung, *Nano letters*, 2011, **11**, 5201-5207.
7. I. Chowdhury, M. C. Duch, N. D. Mansukhani, M. C. Hersam and D. Bouchard, Colloidal properties and stability of graphene oxide nanomaterials in the aquatic environment, *Environmental science & technology*, 2013, **47**, 6288-6296.
8. D. Bouchard, X. Chang and I. Chowdhury, Heteroaggregation of multiwalled carbon nanotubes with sediments, *Environmental Nanotechnology, Monitoring & Management*, 2015, **4**, 42-50.
9. M. Elimelech, J. Gregory and X. Jia, *Particle deposition and aggregation: measurement, modelling and simulation*, Butterworth-Heinemann, 2013.
10. D. Li, M. B. Müller, S. Gilje, R. B. Kaner and G. G. Wallace, Processable aqueous dispersions of graphene nanosheets, *Nature nanotechnology*, 2008, **3**, 101-105.
11. P. Sharma and M. R. Das, Removal of a cationic dye from aqueous solution using graphene oxide nanosheets: investigation of adsorption parameters, *Journal of Chemical & Engineering Data*, 2012, **58**, 151-158.
12. X. Mi, G. Huang, W. Xie, W. Wang, Y. Liu and J. Gao, Preparation of graphene oxide aerogel and its adsorption for Cu 2+ ions, *Carbon*, 2012, **50**, 4856-4864.
13. K. Y. Yoon, S. J. An, Y. Chen, J. H. Lee, S. L. Bryant, R. S. Ruoff, C. Huh and K. P. Johnston, Graphene oxide nanoplatelet dispersions in concentrated NaCl and stabilization of oil/water emulsions, *Journal of colloid and interface science*, 2013, **403**, 1-6.
14. J. Luo, L. J. Cote, V. C. Tung, A. T. L. Tan, P. E. Goins, J. Wu and J. Huang, Graphene oxide nanocolloids, *Journal of the American Chemical Society*, 2010, **132**, 17667-17669.
15. L. J. Cote, J. Kim, V. C. Tung, J. Luo, F. Kim and J. Huang, Graphene oxide as surfactant sheets, *Pure and Applied Chemistry*, 2010, **83**, 95-110.
16. Z. Yang, H. Yan, H. Yang, H. Li, A. Li and R. Cheng, Flocculation performance and mechanism of graphene oxide for removal of various contaminants from water, *Water research*, 2013, **47**, 3037-3046.